npj | climate and atmospheric science

www.nature.com/npjclimatsci

ARTICLE OPEN

Check for updates

Rapid growth and high cloud-forming potential of anthropogenic sulfate aerosol in a thermal power plant plume during COVID lockdown in India

Aishwarya Singh[1,2,3], Subha S. Raj[1,2], Upasana Panda[1,4], Snehitha M. Kommula[1,2], Christi Jose[1,2], Tianjia Liu[5], Shan Huang[6], Basudev Swain[7], Mira L. Pöhlker[8], Ernesto Reyes-Villegas[9,10], Narendra Ojha[11], Aditya Vaishya[12], Alessandro Bigi[13], R. Ravikrishna[2,14], Qiao Zhu[15], Liuhua Shi[15], James Allen[9,16], Scot T. Martin[5,17], Gordon McFiggans[9], Meinrat O. Andreae[8,18,19], Ulrich Pöschl[8], Hugh Coe[9], F. Bianchi[20], Hang Su[8], Vijay P. Kanawade[21], Pengfei Liu[3]✉ and Sachin S. Gunthe[1,2]✉

The COVID lockdown presented an interesting opportunity to study the anthropogenic emissions from different sectors under relatively cleaner conditions in India. The complex interplays of power production, industry, and transport could be dissected due to the significantly reduced influence of the latter two emission sources. Here, based on measurements of cloud condensation nuclei (CCN) activity and chemical composition of atmospheric aerosols during the lockdown, we report an episodic event resulting from distinct meteorological conditions. This event was marked by rapid growth and high hygroscopicity of new aerosol particles formed in the SO_2 plume from a large coal-fired power plant in Southern India. These sulfate-rich particles had high CCN activity and number concentration, indicating high cloud-forming potential. Examining the sensitivity of CCN properties under relatively clean conditions provides important new clues to delineate the contributions of different anthropogenic emission sectors and further to understand their perturbations of past and future climate forcing.

npj Climate and Atmospheric Science (2023)6:109 ; https://doi.org/10.1038/s41612-023-00430-2

INTRODUCTION

The accurate quantification of aerosols responsible for climate-forcing relative to the preindustrial era is crucial for estimating the climate impacts caused by the current anthropogenic enhancement of the atmospheric aerosol burden[1,2]. The aerosol climate forcing associated with changes in cloud albedo depends not only on the enhancement of anthropogenic aerosol concentration but also on the baseline concentration from natural emissions[3]. Under relatively clean conditions, the cloud condensation nuclei (CCN) concentration, the cloud droplet concentration, and the cloud albedo effect are more sensitive to an increase in anthropogenic emissions than under heavily polluted conditions[3]. Therefore, the uncertainty in climate forcing estimates is often linked to a lack of knowledge about aerosol concentrations and properties under relatively clean environments, as well as background conditions before industrialization[4]. However, our knowledge in this regard largely relies on chemistry-climate modeling rather than measurements because of the pervasive pollution conditions with pollutants from complex sources that typically prevail today, especially in India. Given the highly non-linear response of cloud properties to aerosol concentration and the complexity of emission sources, additional measurements in relatively cleaner conditions with reduced anthropogenic emissions can help unravel how precursor emissions, aerosol formation and growth, and aerosol properties, including number concentration and chemical composition, impact cloud condensation nuclei concentrations and climate forcing through aerosol-cloud interactions[3,5–11].

During the COVID lockdown in India, an interesting scientific opportunity presented itself during the transition from heavily polluted to relatively cleaner conditions. The pandemic outbreak of coronavirus (COVID-19) affected more than 10 million people across India[12–14]. To contain the domestic spread of COVID-19, India imposed a nationwide lockdown beginning on 25 March 2020, limiting the economic activity of 1.3 billion people and leading to significant reductions in anthropogenic emissions until 31 May 2020[15]. The lockdown caused a drastic reduction in major local anthropogenic emissions, such as those from traffic and industrial sources, as evident from decreasing concentrations of major pollutants, including PM_1, $PM_{2.5}$, and black carbon (BC)

[1]EE Division, Department of Civil Engineering, Indian Institute of Technology Madras, Chennai, India. [2]Centre for Atmospheric and Climate Sciences, Indian Institute of Technology Madras, Chennai, India. [3]School of Earth and Atmospheric Sciences, Georgia Institute of Technology, Atlanta, GA, USA. [4]Department of Environment and Sustainability, CSIR – Institute of Minerals and Materials Technology, Bhubaneswar, India. [5]Department of Earth and Planetary Sciences, Harvard University, Cambridge, MA, USA. [6]Institute for Environmental and Climate Research, Jinan University, Guangzhou, Guangdong, China. [7]Institute of Environmental Physics, Department of Physics, University of Bremen, Bremen, Germany. [8]Multiphase Chemistry Department, Max Planck Institute for Chemistry, Mainz, Germany. [9]Department of Earth and Environmental Sciences, School of Natural Sciences, University of Manchester, Manchester, UK. [10]Tecnologico de Monterrey, Escuela de Ingeniería y Ciencias, Av. General Ramon Corona 2514, Nuevo México, Zapopan CP 45138 Jalisco, Mexico. [11]Space and Atmospheric Sciences Division, Physical Research Laboratory, Ahmedabad, India. [12]School of Arts and Sciences and Global Centre for Environment and Energy, Ahmedabad University, Ahmedabad, India. [13]Dipartimento di Ingegneria 'Enzo Ferrari', University of Modena and Reggio Emilia via Vivarelli, Modena, Italy. [14]Department of Chemical Engineering, Indian Institute of Technology Madras, Chennai, India. [15]Gangarosa Department of Environmental Health, Rollins School of Public Health, Emory University, Atlanta, GA, USA. [16]National Centre for Atmospheric Science, University of Manchester, Manchester, UK. [17]John A. Paulson School of Engineering and Applied Sciences, Harvard University, Cambridge, MA, USA. [18]Scripps Institution of Oceanography, University of California San Diego, La Jolla, CA, USA. [19]Department of Geology and Geophysics, King Saud University, Riyadh, Saudi Arabia. [20]Institute for Atmospheric and Earth System Research/Physics, University of Helsinki, Helsinki, Finland. [21]Center for Earth, Ocean, and Atmospheric Sciences, University of Hyderabad, Hyderabad, India. ✉email: pengfei.liu@eas.gatech.edu; s.gunthe@iitm.ac.in

across India[16–26]. While there was an overall change from heavily polluted to relatively cleaner conditions due to curtailed anthropogenic emissions, some anthropogenic sectors, such as the power industry, a major emitter of SO_2, continued to operate normally during this lockdown period. This setup offered an interesting scientific opportunity to isolate the effects of the thermal power production industry from the normally entwined activities of other industries and transportation on regional pollution. It further allowed studying the sensitivity of CCN concentrations in response to the differential reductions in different anthropogenic sectors. The impact of SO_2 emissions from coal-fired power plants on aerosol processes under relatively cleaner conditions could be studied with reduced interference from other anthropogenic sources.

In this context, the coastal city of Chennai experienced a substantial reduction in local anthropogenic pollution[18]. On the other hand, the Neyveli coal-fired power plant, located ~200 km south of our observational site in Chennai, continued full operation during the COVID lockdown. This power plant has an installed capacity of 3390 MW as of April 2021 and produces 2740 MW of electricity from its three operational units, emitting 299 kt SO_2 a^{-1} [27]. Being one of India's largest coal-fired power plants, the Neyveli plant is arguably the most significant point source for the emission of SO_2 and NO_x, among other air pollutants, in the southern part of the nation[27,28]. The electrostatic precipitators installed at the stacks of this power plant effectively curb the primary particulate emissions to a great extent. However, if, as stated in recent reports[28,29], flue gas desulfurization (FGD) systems for SO_x control and/or catalytic degradation systems for NO_x control are not installed at most of its units, the measures for controlling SO_2 and other gaseous pollutants would appear to be inadequate[28,29].

Here, we report a case study for a new particle formation and growth event triggered by the long-range transport of SO_2 emitted from the Neyveli thermal power plant. The associated chemical and cloud-forming properties of ambient aerosols were analyzed based on comprehensive aerosol measurements from Chennai, carried out during the COVID lockdown. When the power plant plume intersected the observation site, there were high sulfate concentrations and associated new particle formation, which was followed by rapid particle growth. The sulfate-rich particles rapidly grew into CCN size, and were observed to have high hygroscopicity, thus largely increasing the CCN concentration. The observations and analysis presented herein provide a rare opportunity to examine the sensitivity of CCN to new particle formation and growth due to SO_2 emissions from a coal-fired power plant under relatively cleaner conditions for tropical India, thereby establishing a baseline for comparison and contrast against the usually prevailing conditions of heavy pollution. The frequently used notations, symbols, and abbreviations are listed in Supplementary Table 1.

RESULTS AND DISCUSSION

Variations in aerosol properties over Chennai during the COVID lockdown

The COVID lockdown in India during March–May 2020 led to a drastic decrease in the overall anthropogenic emissions across the country[16–26]. Compared to the usual pollution levels, a significant reduction in the overall aerosol burden over the south Indian region was also observed (Fig. 1a, b). The relative difference between the aerosol optical depth (AOD) values for the campaign duration in 2020, with respect to the same period in 2019, is shown in Supplementary Fig. 1. The time series of NR-PM_1 (non-refractory particulate matter with diameters ≤1 µm), SMPS-$PM_{0.5}$ (particulate matter with diameters ≤0.5 µm, derived from Scanning Mobility Particle Sizer measurements), $PM_{2.5}$ (particulate matter with aerodynamic diameters ≤2.5 µm) and BC measured at Chennai during the COVID lockdown period are shown in Fig. 1. These measurements were carried out between 11 April 2020 and 6 May 2020. The BC concentrations, an indicator of combustion and pollution[30], persistently remained below 5 µg m^{-3} during the measurement period due to the COVID-induced lockdown (average concentration 1.5 ± 0.7 µg m^{-3}; Fig. 1c). In contrast, for a similar period before lockdown during the business-as-usual scenario, the average concentrations were ~3-4 times higher (5.4 ± 11.9 µg m^{-3}; Supplementary Fig. 2) and exhibited a pronounced diurnal variation with a strong morning peak, suggesting elevated local emissions. In comparison, the observed weak average diurnal variation (Supplementary Fig. 2) in BC concentrations during the lockdown suggests significantly reduced combustion-related anthropogenic activities. Other than anthropogenic sources, wildfires and open burning are major primary sources of atmospheric BC, and their widespread occurrences result in transport and persistent presence, even in the remote marine and continental boundary layer[31]. These sources, along with residential emissions, may shape the regional background of BC observed during the COVID lockdown. Looking more in detail at the lockdown period, the weak correlation between SMPS-$PM_{0.5}$ and BC ($R^2 = 0.18$, Supplementary Fig. 3) indicates that local combustion sources, such as traffic and industrial emissions, played a minor role in determining the overall PM pollution level. The average aerosol properties and meteorological parameters for the campaign period are summarized in Supplementary Table 2.

New particle formation and growth event

Interestingly, on 1 May, a day dominated by prevalent southerly winds (Fig. 2a) and relatively low average BC concentration (1.9 ± 0.7 µg m^{-3}; Fig. 1c), NR-PM_1, and SMPS-$PM_{0.5}$ mass concentrations reached ~40 µg m^{-3} (Fig. 1c), with corresponding $PM_{2.5}$ concentration reaching ~40–50 µg m^{-3} as evident in Fig. 1d (marked by the golden shaded region). The strong correlation between SMPS-$PM_{0.5}$ and NR-PM_1 (Fig. 1e; $R^2 = 0.8$; $N = 92$) and a relatively weak correlation between SMPS-$PM_{0.5}$ and BC ($R^2 = 0.18$ during the event; Supplementary Fig. 3) indicates the relatively low contribution of local combustion-related anthropogenic sources to the total aerosol mass burden on 1 May. The observed increase in total aerosol mass burden coincided with a large-scale increase in the number concentration of ultrafine particles (Fig. 2c, d). This increase in concentrations of ultrafine particles appears to have resulted from atmospheric new particle formation from gaseous precursors, as discussed below.

New particle formation (NPF) on this day was triggered after sunrise (05:49 local time, LT) in the continental air mass (Fig. 2b–d) with a sustained and rapid increase in total particle number concentrations (N_{Tot}) and geometric median diameter (D_{gmd}) until 11:30 LT. At around 11:30 LT, however, a break in the growth event was noticed, potentially caused by an abrupt and prominent transition of air masses (Fig. 2b), and as a result, the aerosol size distribution appears as a broken banana-shaped aerosol growth (Fig. 2d), similar to growth events reported from other sites in previous studies[32–34].

From midnight till noon, the chemical composition of PM_1 (NR-PM_1 from ACSM + BC from AE-33) was dominated by organic aerosols (Org) followed by sulfate (SO_4), ammonium (NH_4), and nitrate (NO_3) (Fig. 2c and Supplementary Fig. 4; Org: 57%, SO_4: 31%; NH_4: 8%, and NO_3: 3%), exhibiting the typical moderately polluted regional conditions. The increase in organics in the morning around 07:00 LT (Fig. 2d) is likely due to the downward mixing of this regional air mass into the deeper moist coastal boundary layer during the day rather than local emissions[35,36]. Following the abrupt transition of air mass from the south-westerly to southerly/south-easterly direction, the sulfate concentration increased ~1.5-fold (Fig. 2c, Supplementary Fig. 4). This

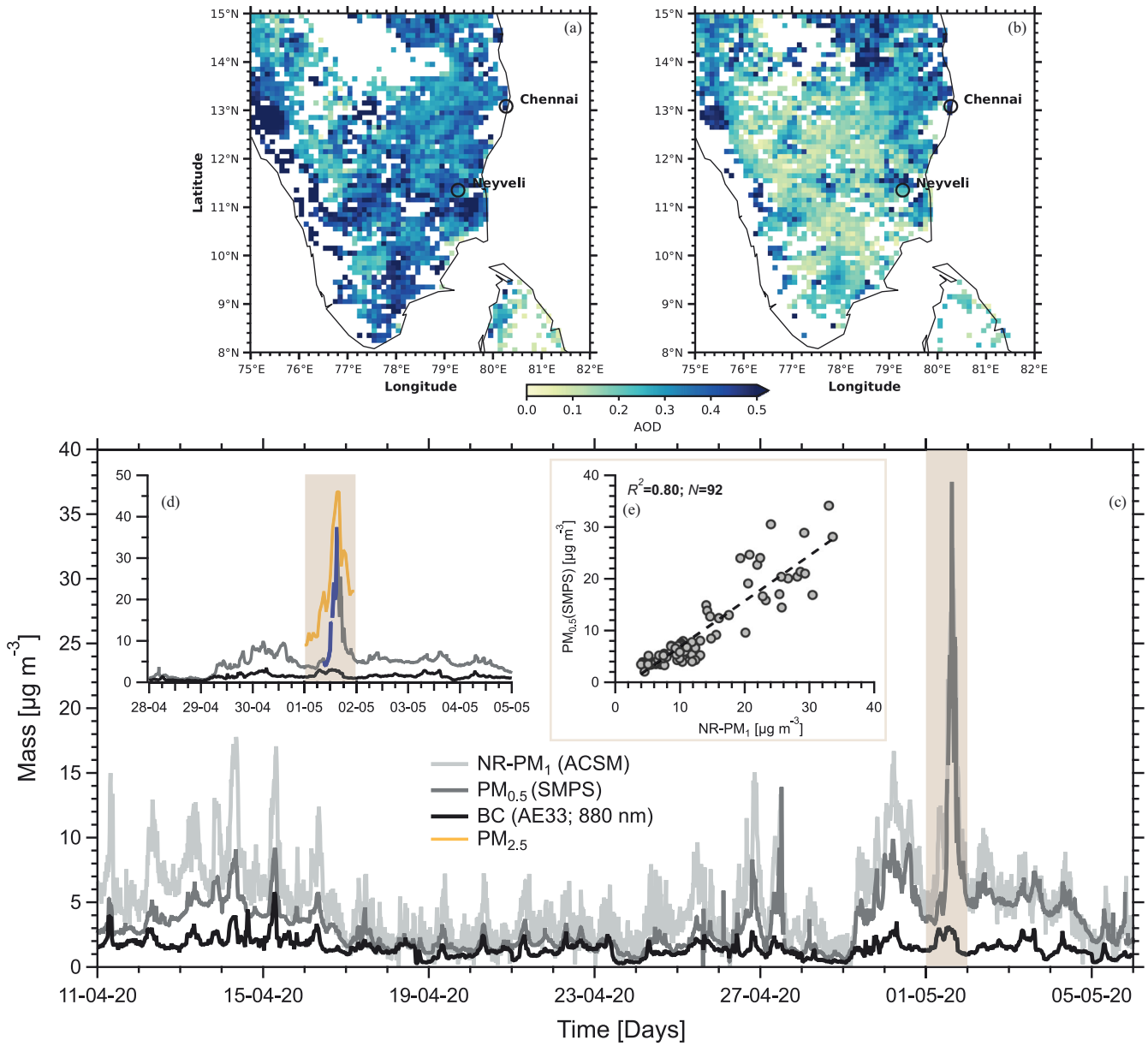

Fig. 1 Measurements of particulate matter concentrations ($PM_{0.5}$, NR-PM_1, $PM_{2.5}$, and black carbon), measured between 11 April and 6 May 2020 in the coastal city of Chennai during the COVID-19 lockdown. a Map showing the location of Chennai and the Neyveli Power Plant (NPP), color scaled with MODIS Level-2 AOD (Aerosol Optical Depth), averaged between 28 March and 5 May 2019, the time of the year equivalent to that of the COVID-19 lockdown in India in 2020. The relative difference in AOD is shown in Supplementary Fig. 1. **b** Same as (**a**) but for the year 2020. **c** Time series of Non-Refractory PM_1 (NR-PM_1) mass from ACSM, mass concentration derived from SMPS (SMPS-$PM_{0.5}$) number size distribution measurements in the size range of ~10–450 nm and converted to mass concentration assuming a density of 1.1 g cm^{-3}, and black carbon concentration as measured by Aethalometer, for the campaign duration from 11 April 2020 to 6 May 2020. The light golden shading in panel (**c**) indicates the NPF and rapid particle growth event day. **d** Mass concentrations of NR-PM_1, SMPS-$PM_{0.5}$, and U.S. Embassy $PM_{2.5}$ for 8 days. The extremely high concentration observed on 1 May is highlighted in blue color. **e** Scatter plot between NR-PM_1 and SMPS-$PM_{0.5}$ for the event day, indicating the high mass concentration detected by both measurement techniques.

implies that a high amount of sulfate in the southerly air mass resulted in an exceptionally high fraction of sulfate in the total aerosol mass burden during the particle growth.

The rapid aerosol particle growth event at this site indicates greater availability of low-volatility vapors for aerosol nucleation and growth under cleaner conditions, which pre-existing aerosol particles would otherwise scavenge[37]. This is evident in Fig. 2f, showing a low condensation sink of 5×10^{-3} s^{-1} before the rapid growth event. Remarkably, an increase in the SO_4:Org ratio from ~0.2 before the onset of the NPF event to three-fold higher by the end of the particle growth event indicated a significant contribution of sulfate to the aerosol growth that formed particles in the accumulation mode (Fig. 2c). This is in contrast with previous observations from numerous other locations showing the dominance of the organic fraction in nanoparticle growth[38–43]. Several NPF events recorded at this site under business-as-usual conditions of high pollution also exhibited a dominance of organics in particle growth. A detailed comparison of differences in nucleation mechanisms during such events will be presented in follow-up studies.

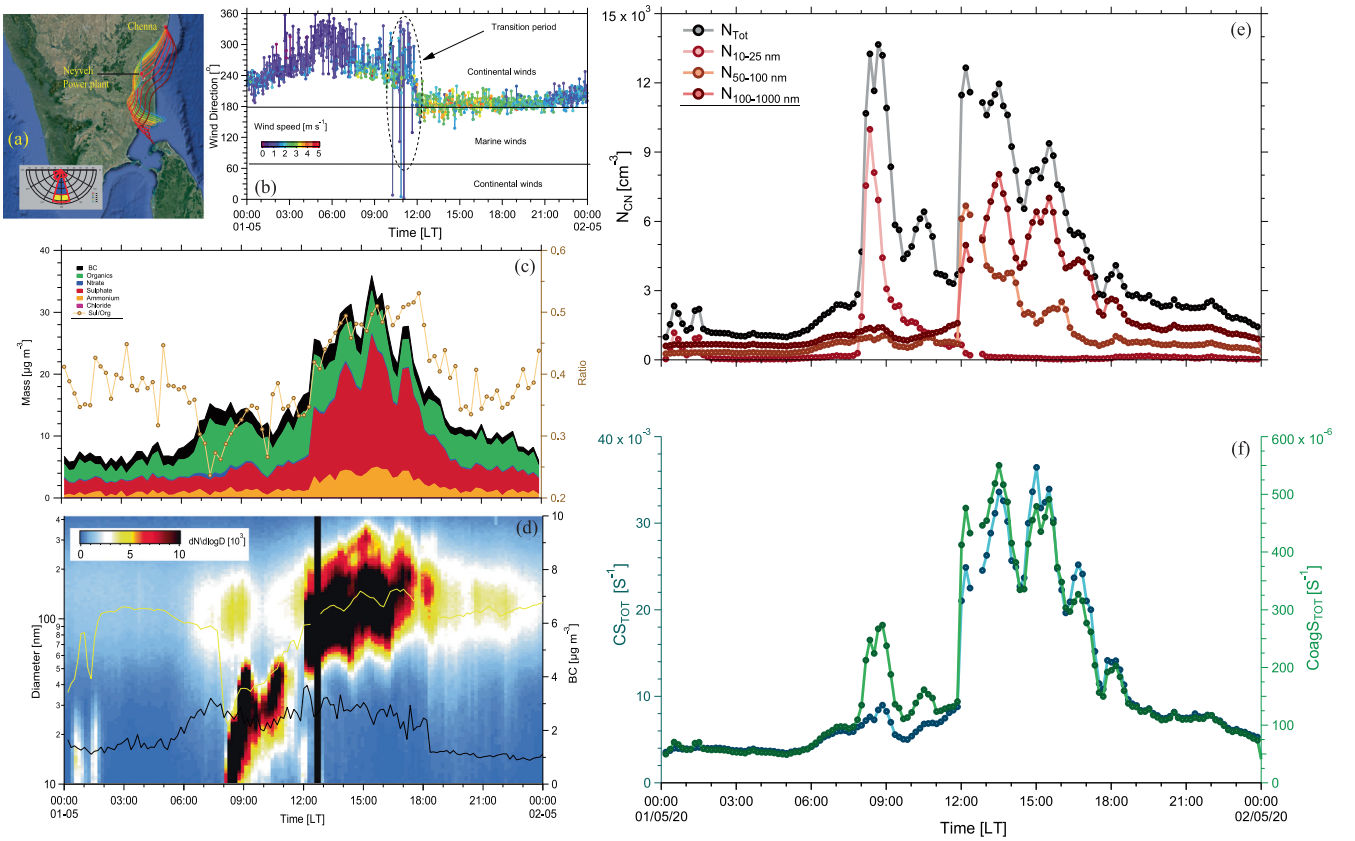

Fig. 2 Various aerosol characteristic properties and meteorological conditions observed and derived for 1 May 2020 on the day of the rapid particle growth event. a 48-h backward-trajectories obtained for each hour between 06:30–18:30 LT and automatic weather station data (inset), indicating predominant southerly winds. **b** Time series of wind direction color coded by the wind speed. The transition period is marked with a dashed circle. **c** Time series showing the variations in chemical components in PM_1 measured on the event day. On the same plot, the orange line indicates the variation in the sulfate:organic ratio measured by ACSM. **d** Sub-micrometer particle number size distribution measured by SMPS showing rapid particle growth during the event (local time plotted against diameter and scaled by normalized particle number concentration). The yellow line indicates the geometric median diameter of the mode fitted to the number size distribution, and the black line shows the black carbon concentration, which remained <4 µg m^{-3} throughout the event. **e** Size segregated particle number concentration as measured by SMPS over the entire measured diameter range (N_{Tot}), over 10–25 nm ($N_{10–25}$), over 50–100 nm ($N_{50–100}$), and over 100–1000 nm ($N_{100–1000}$). **f** Total condensation and coagulation sink during the growth event day.

Potential mechanisms and sources of high-sulfate particulate matter

To explore the possible origin of the observed sulfate particles, we calculated the associations of the BC+Org fraction (proxy of local combustion emissions) and SO_4 fraction with NR-PM_1 + BC (i.e., PM_1) concentrations. We found a negative association of BC+Org with PM_1, whereas SO_4 was positively associated with PM_1, which is usually the opposite for the business-as-usual scenario (Supplementary Fig. 5). These results, combined with the persistent high SO_4 concentration after the change in wind direction, indicate that the observed SO_4 was not emitted from local sources, and the observations may represent broader regional conditions.

The most likely source is SO_2 emissions from the Neyveli thermal power plant, located nearly 200 km south of the measurement site. This coal-fired power plant, which has been estimated to emit about 300 kt SO_2 a^{-1} [27], continued full operation during the COVID lockdown. In the downwind plumes from coal-fired power plants, SO_2 can undergo rapid oxidation to produce sulfate aerosol[37] and, because the efficient combustion process in power plants releases relatively little BC and organics (photographs of the Neyveli power plant show no black smoke emanating from the stacks), their emissions result in Sulfate:BC ratios much higher than from diesel trucks, biomass burning, etc. Nucleation events resulting from H_2SO_4 and water produced from SO_2 oxidation in power plant plumes under similar meteorological conditions have been reported previously[44].

The STILT model simulations, which were carried out for the entire measurement period to investigate the footprint area affecting our observation site, indicated the SO_2 sensitivity to both continental and marine regions with a relatively lower aerosol mass burden (Fig. 3a). In addition, satellite SO_2 imagery clearly indicated the dispersion and large-scale transport of the SO_2 plume from the Neyveli power plant over this region, including the observational site throughout the measurement period (Fig. 3d). On the growth event day, particularly during 08:00–18:00 LT, air mass back-trajectory analysis (Fig. 2a), along with the STILT sensitivity analysis, TROPOMI satellite imagery, and HYSPLIT dispersion modeling results showed strong sensitivity of the measurement site to SO_2 emissions originating from the south/southeast direction (Fig. 3b, c, e, f). These observations support the scenario that the SO_2 plume emitted from the Neyveli power plant situated southeast of the observational site (Fig. 3f) contributed to the high sulfate in the particulate matter measured at this observational site.

The observed new particle formation and growth event associated with high SO_4 strongly coincided with unique meteorological conditions. An abrupt and prominent transition of the air mass from south-westerly to south/south-easterly direction occurred at around 11:30 to 12:00 LT (Fig. 2b). However,

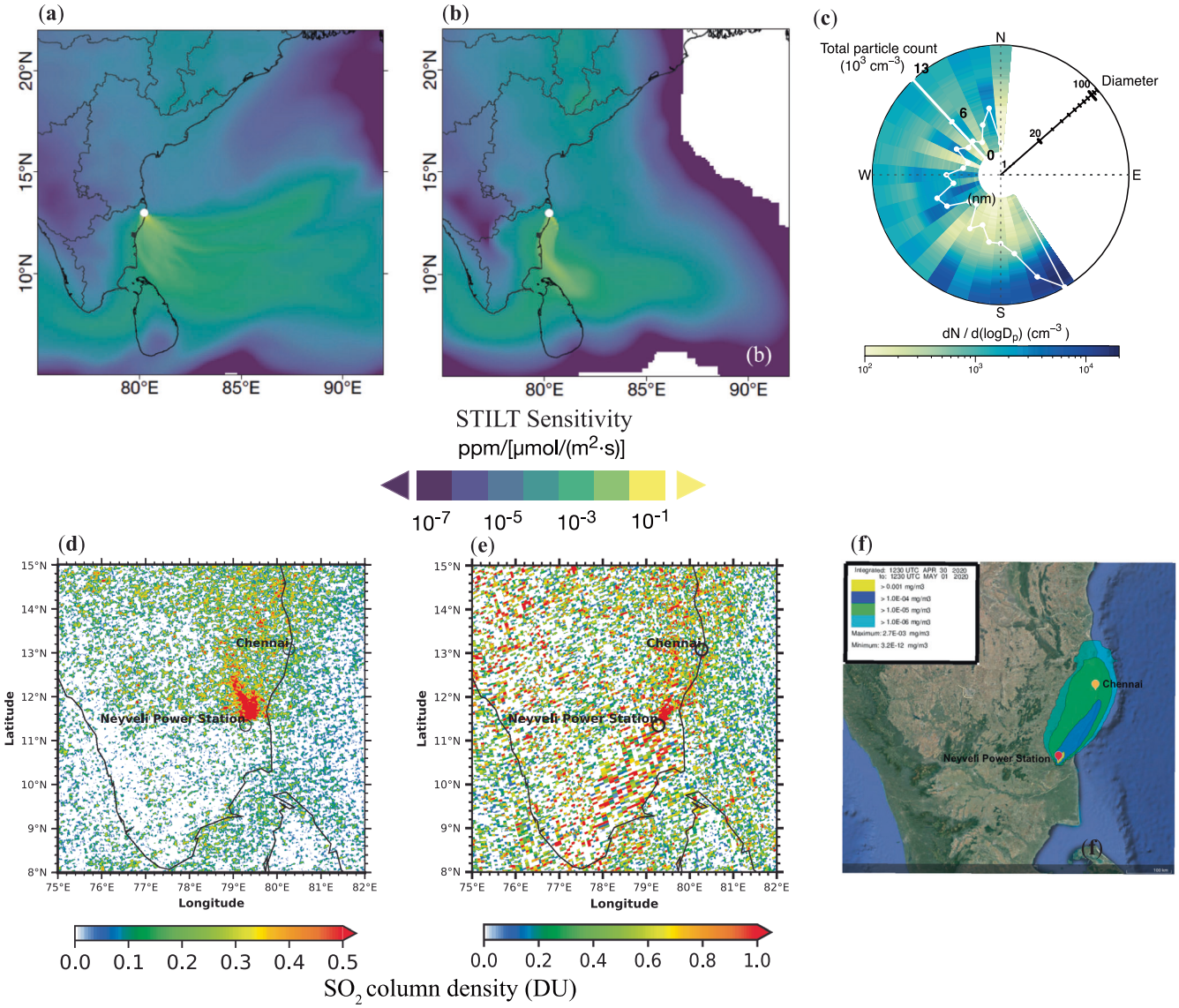

Fig. 3 Sensitivity of the measurement site with respect to nearby potential emission sources. The sensitivity presented here is derived using the Stochastic Time-Inverted Lagrangian Transport (STILT) model. **a** Sensitivity during the entire measurement period during the lockdown. **b** For 1 May when the particle growth event was observed. The STILT model was driven with meteorological data obtained from the Global Data Assimilation System (GDAS) with a spatial resolution of 0.5 × 0.5 degrees. The corresponding back trajectory footprint was resampled at a finer resolution of 0.01 × 0.01 degrees. Note that the color bar is on a logarithmic scale. **c** Particle number size distribution for 1 May binned according to wind direction. The black line indicates the diameter on a logarithmic scale, and the white line shows the total particle concentration corresponding to each wind direction bin. **d** SO_2 column density as obtained from TROPOMI satellite averaged over the campaign period. **e** Same as (**d**) but averaged over 30 April and 1 May. **f** NOAA HYSPLIT dispersion model run in forward mode showing the plume from Neyveli power plant reaching the observational site for 1 May.

the back-trajectories for the event period indicate that both air masses, before and after the wind direction change, originated in the south, potentially passing over the power plant. Trajectories after midday appeared to have taken longer to cover the distance between the power plant and the observational site because of a less direct transport path (Fig. 2a and Supplementary Table 3), which explains the high concentration of sulfate particles in the accumulation mode. We further derived estimations of backward distance, mixed layer depth, trajectory height, and potential temperature of the 48-h backward air mass trajectories, which crossed the power plant area and eventually arrived at the receptor site (refer to Supplementary text). For the representation purpose, we specifically focused on the time periods when the air masses reached the receptor site before and during the growth event (Supplementary Fig. 6a). As depicted in Supplementary Fig. 6a, the backward trajectories demonstrated an increased mixed layer depth of ~700 meters when the airmass was close to the power plant. This suggests that the air masses likely picked up SO_2 emissions while passing over the power plant. However, as the air masses continued to travel, it was observed that the mixed layer depth decreased to less than ~200 meters after ~50 km. This reduction in mixed layer depth, in combination with trajectory height always remaining within the mixed layer, hindered the dispersion, potentially resulting in the SO_2 being retained in the air mass as it traveled toward the receptor site. Upon reaching the receptor site, a systematic and significant evolution in the mixed layer depth as the day progressed led to the vertical mixing of the sulfate aerosol within the daytime boundary layer (Supplementary Fig. 6a). With the support of these findings, we hypothesize that the rapid particle growth, with high particulate sulfate mass

fraction, was highly likely either formed or enhanced by the condensation of H_2SO_4 resulting from the oxidation of SO_2 contained in the plume during the air masses' journey from the point source to the receptor site. As a result of the transition period, there was a transient decrease in the number of aerosol particles and mass concentrations; however, the rapid growth of the newly formed particles was observed to continue after 12:00 LT until 18:00 LT, exhibiting the typical characteristics of an NPF and growth event (Fig. 2d).

The analysis of the air mass backward trajectory and the variations of mixed layer depth along the airmass path leading to the receptor site during the event indicate the direct transport of a well-mixed power plant plume to the receptor site (Fig. 2a and Supplementary Fig. 6a). Conversely, on the other days with comparatively higher aerosol mass concentration (albeit with an aerosol mass burden less than on the event day) throughout the measurement period, dominant marine air masses were observed reaching the receptor site. Supplementary Figs. 6c and d present the backward trajectory analyses and mixed layer depth variations of one such notable day (14 Apr 2020; PM_1 mass ~20 μg m^{-3}).

The reduced number concentration of pre-existing aerosol particles due to reduced anthropogenic emissions during lockdown seems to have enhanced the new particle formation and growth observed during this study. A lesser concentration of pre-existing aerosol particles implies a lower condensation sink (CS) for H_2SO_4 condensation, leading to enhanced ultrafine particle formation through nucleation. It has been previously reported that only a small fraction of the H_2SO_4 condenses onto the pre-existing particles, while 90% condenses onto the newly-formed particles under cleaner marine conditions[37]. This leads to the sustained growth of nucleated particles to larger sizes, as observed in the present study. However, it is critical to note that condensation of H_2SO_4 alone may not be sufficient to explain the exceptionally high growth rates of the newly formed particles (~20 nm h^{-1} for particles above 50 nm in diameter) observed during this event[45]. Size-resolved growth rates for the rapid particle growth event observed on 1 May are summarized in Supplementary Table 4. The size-growth of the "sulfate-rich" particles may have also resulted from increasing heterogeneous uptake of SO_2 with increasing RH and particle diameter as the day progressed, especially after 12:00 LT (Fig. 2d and Supplementary Fig. 6b). Several previous studies at urban sites have indicated that sulfate increased quicker with elevated RH and particle diameter than organics[46,47].

We also explored the possibility that the growth event and high particulate sulfate at our coastal location could have been triggered by precursors resulting from biogenically emitted dimethyl sulfide (CH_3SCH_3; DMS) oxidation. Methane sulfonic acid (CH_3SO_3H; MSA) has been used as a proxy for DMS using online mass spectrometry measurements[48,49]. The biogenically emitted DMS from open oceans undergoes oxidation to form H_2SO_4 and MSA, leading to aerosol nucleation and growth. Given the limitation of unit mass resolution, we did not find any evidence of enhancement in *m/z* 79, representing MSA, from the ACSM data. Since the MSA:nssSO_4 ratio can be quite low (<0.1) even in clean marine conditions[50], the lack of detectable MSA is not a conclusive evidence against a contribution from biogenic DMS. However, to produce such a high sulfate concentration would require an even greater concentration of DMS, which would exceed the highest DMS concentration ever reported, and therefore a significant source originating from oceanic emissions is ruled out in this case.

Variations in aerosol number and mass concentration during the event

The number concentration for particles in the size range of 10–25 nm diameter ($N_{10–25\ nm}$) started to increase approximately at 08:00 LT local time, reaching as high as ~10,000 cm^{-3} within about 20 min, contributing 77% to the total measured number concentration (N_{Tot}), which likewise increased by five times (from ~2500 cm^{-3} to ~13,000 cm^{-3}; Fig. 2e). The increase in $N_{50–100\ nm}$ and $N_{100–1000\ nm}$ (accumulation mode particles) was observed later during the aerosol growth event, consistent with previous studies reporting NPF and particle growth events[51–53]. However, the chemical composition of the newly formed particles in the Aitken mode cannot be ascertained as the ACSM is unsuitable for characterizing particles smaller than ~50 nm. The increase in sulfate concentration recorded by the ACSM, which coincided with the increase in particles in the $N_{50–100\ nm}$ and $N_{100–1000\ nm}$ size ranges, mainly represents the increasing sulfate mass fraction for particles between ~70–700 nm, as the collection efficiency of the instrument is optimum in this range[54]. As evident from Fig. 2d, for a brief period at the start of the NPF event, we observed a bimodal aerosol number size distribution with modal diameters of <30 nm and ~100 nm. It may be noted that since the ACSM cannot account for the chemical composition of particles <50 nm, which could be sulfate-rich in nature, we could not observe the changes in the chemical mass composition of nucleation mode particles, which may also be dominated by organics. Once the newly formed sulfate-rich particles grew, reaching ~70 nm, and the aerosol number size distribution became unimodal, a substantial increase in sulfate mass fraction was observed (Fig. 2c, d).

The balance between precursor concentrations and pre-existing particle loading decides when new particle formation will be triggered in the atmosphere[55,56], and the interplay of condensation sink (CS) and Coagulation sink (CoagS) determines the balance between particle formation, growth, and removal. The coagulation sink (CoagS) in the NPF event observed on 1 May is about two orders of magnitude lower than the condensation sink (CS), indicating a less significant loss of newly formed particles to pre-existing aerosols, which were low in number under the lockdown-induced cleaner conditions. The CS sharply increased by about a factor of 4 after 12:00 LT due to a sharp change in air mass and as particles grew to CCN-active sizes (i.e., 50 nm). The growth event, which continued until 18:00 LT, weakened in terms of the particle concentration with N_{Tot}, $N_{10–25\ nm}$, $N_{50–100\ nm}$, and $N_{100–1000\ nm}$ reaching 5000 cm^{-3}, <50 cm^{-3}, 2500 cm^{-3}, and 4000 cm^{-3}, respectively. The SO_4:Org ratio started to decrease at 18:00 LT, coinciding with the end of the growth event (Fig. 2c). The D_{gmd} increased consistently during the event, increasing from ~20 nm to as high as ~160 nm, not as a constant growth but as the appearance of a new mode around noon. Very few studies have reported such a significant and rapid growth in D_{gmd} during a growth event[52,57]. A study in Beijing reported that a high amount of freshly nucleated nanoparticles from organic precursors during a clean period often precedes episodes of high pollution due to the growth of these nanoparticles to bigger sizes leading to increased aerosol mass burden. In the same study, it was also observed that the local sulfate and nitrate emissions further enhanced the rapid growth of the newly formed particles[57]. In our case, the increased concentration of larger-sized particles could likely be attributed to relatively aged sulfate-rich particles that had formed while the air mass traveled from the point source to the receptor site.

Role of sulfate in high cloud-forming potential

Nevertheless, regardless of the potential sources accountable for the rapid growth of particles, we observed strong implications for cloud formation, as evident from the evolution of the aerosol number size distribution and CCN concentration (Fig. 4a–c). At the onset of the NPF event, particles were very small ($D_{gmd} \cong 15$ nm), and accumulation mode particles already present in the atmosphere dominated the CCN number concentration. Thereafter, the aerosol particles exhibited rapid growth with an increase in the sulfate fraction, with D_{gmd} reaching as high as ~160 nm and a sulfate fraction exceeding 50% (Fig. 4e) in NR-PM_1. At the lowest effective supersaturation ($S_{eff} = 0.15\%$ and average $D_{50} = 138 \pm 14$ nm), the modal diameter of the CCN distribution

continued to be unaffected, while the sulfate fraction of PM_1 increased from ~20 to 60% (Fig. 2c). Compared with the measurements conducted before and after the NPF event, the hygroscopicity parameter κ measured at $S_{eff} = 0.15\%$ during the event increased from 0.22–0.25 to 0.53 (Fig. 4b). The effect of the increase in N_{CN} and particle size on N_{CCN} is summarized in Supplementary Table 5. At the highest $S_{eff} = 0.79\%$, while the aerosol size distribution was dominated by the accumulation mode from the onset of the rapid particle growth, the CCN number concentrations increased in the Aitken mode during the event (Fig. 4c). A significant increase in κ was also observed for $S_{eff} = 0.79\%$ (Fig. 4c). Similar observations were previously

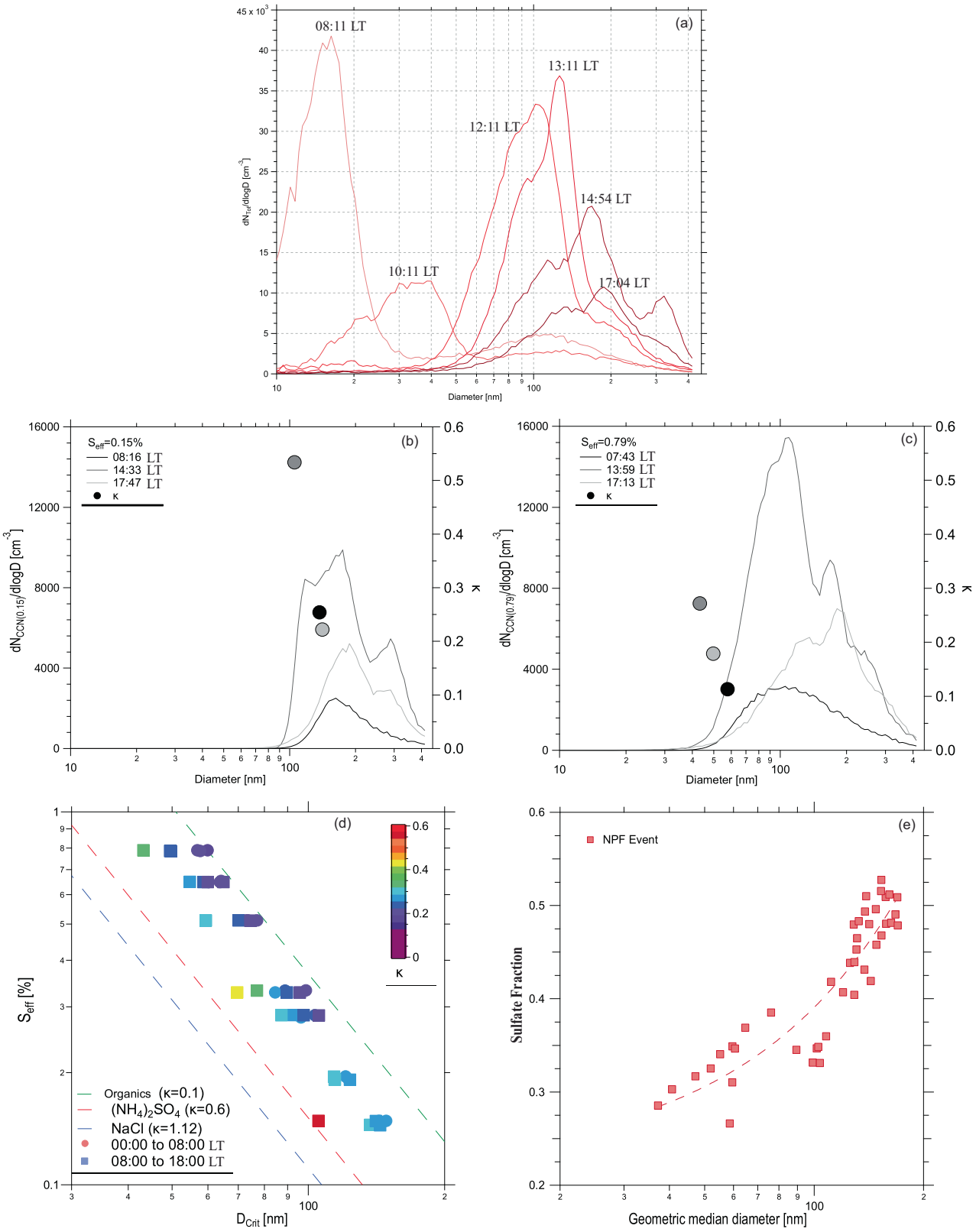

Fig. 4 Various characteristic aerosol properties derived using size-resolved CCN, ACSM, and SMPS measurements on the day of the NPF and rapid particle growth event at Chennai. a Particle number size distribution (normalized particle concentration in cm^{-3} plotted against diameter in nm). The individual aerosol number size spectra obtained from SMPS measurements plotted represent the time of the day before, during, and after the particle growth event. **b** Same as (**a**) but for CCN number size distribution derived for 0.15% effective supersaturation. **c** Same as (**a**) but for CCN number size distribution derived for 0.79% effective supersaturation. The markers in (**b**) and (**c**) represent the hygroscopicity parameter Kappa (κ), calculated from size-resolved CCN measurements for corresponding CCN number size distribution of 0.15% and 0.79% effective supersaturation, respectively. In panels (**b**) and (**c**), CCN number size distributions and κ are color coded by the time of the day. **d** The relation between critical dry diameter, D_{crit} (nm), and effective supersaturation, estimated from size-resolved CCN measurements. The different marker shapes represent the time before (circle) and during (square) the particle growth event. These different markers are further color coded by κ calculated using the individual pairs of D_{crit} (nm) and effective supersaturation on the day of the particle growth event. **e** Scatter plot between geometric median diameter of the mode fitted to the number size distributions measured by SMPS and the sulfate fraction measured by ACSM ($N = 42$ and $R^2 = 0.85$). The dotted red line is a linear fit to the points.

reported from an urban site in Beijing[58]. The rapid aerosol particle growth, which was associated with a high sulfate fraction, clearly indicated the high cloud-forming ability in terms of the higher κ, particularly for Aitken and accumulation mode particles (Fig. 4d). The role of increasing diameter for higher cloud-forming ability in this case strongly appeared to be coinciding with the increase in sulfate fraction (Fig. 4e). Overall, the increase in sulfate fraction clearly showed a positive association with increasing κ values.

To further investigate the impact of increasing N_{CN}, aerosol size, and changing chemical composition on N_{CCN}, we performed sensitivity analyses by estimating the N_{CCN} for different scenarios. For this sensitivity analysis, we considered N_{CCN} derived prior to the event using exemplary aerosol size distributions (07:43 LT and 08:16 LT for $S_{eff} = 0.79\%$ and $S_{eff} = 0.15\%$, respectively) and CCN-efficiency spectra fit parameters as a baseline case[59]. For the baseline scenario, N_{CCN}/N_{CN} was 0.62 and 0.05 for $S_{eff} = 0.79\%$ and $S_{eff} = 0.15\%$, respectively. For the first scenario, we used the CCN-efficiency spectra fit parameters from the growth event corresponding to higher κ (Supplementary Table 6) values, but aerosol number size distribution as of the baseline scenario to predict the N_{CCN} and found a relative difference of 17 and 61% for $S_{eff} = 0.79\%$ and $S_{eff} = 0.15\%$, respectively. Further, we predicted the N_{CCN} by taking the exemplary aerosol number size distributions during the growth event (13:59 LT and 14:33 LT for $S_{eff} = 0.79\%$ and $S_{eff} = 0.15\%$, respectively), but CCN-efficiency spectra fit parameters corresponding to lower κ values (Supplementary Table 6) from the baseline case. Under this scenario, we found a relative difference of 310 and 299% between baseline and predicted N_{CCN} for $S_{eff} = 0.79\%$ and $S_{eff} = 0.15\%$, respectively. However, the N_{CCN} during the growth event was found to be higher by 313 and 429% for $S_{eff} = 0.79\%$ and $S_{eff} = 0.15\%$, respectively, with respect to the baseline case. The corresponding CCN activation spectra for the time considered above for N_{CCN} estimation and prediction are shown in Supplementary Fig. 7. Our sensitivity analyses further confirm the findings as reported by the previous studies indicating that aerosol particle number and size are the primary modulators for the variability of the CCN concentration followed by the particle composition and hygroscopicity[58,60–62]. However, for $S_{eff} = 0.15\%$, the change in chemical composition resulted in an increase of 43% in N_{CCN}, highlighting the importance of chemical composition in modulating the CCN activity at lower supersaturation.

In summary, our observations highlighted a unique new particle formation and rapid growth event under the conditions of reduced anthropogenic emissions during lockdown over this tropical coastal environment. We find that the rapid particle growth, triggered by distinct meteorological conditions, strongly coincided with high particulate sulfate mass fraction. Such a high sulfate mass fraction appears to be either formed or grown by the condensation of H_2SO_4 resulting from the oxidation of the SO_2 plume emitted by a large coal-fired power plant located ~200 km south of the observation site. Heterogeneous uptake of SO_2 under high RH conditions may have further aided the growth of the newly formed particles. Under the business-as-usual scenario, such new particle formation and growth driven by high sulfate concentration would be suppressed due to the large pre-existing aerosol surface area from local sources for H_2SO_4 condensation and particle coagulation. The sulfate-rich particles exhibited strong cloud-forming potential over a varying range of supersaturations, with unusually high CCN fractions and κ values higher than those recorded at other times for this location. The chemical composition of aerosols varied more with time than as a function of particle size during the event, due to condensation of large amount of sulfate. Therefore, the hygroscopicity of these aerosols is found to be more dependent on the chemical composition than particle size, indicating enhanced CCN activity due to increased sulfate fraction. These measurements of aerosol composition, growth rate, CCN number concentration, and hygroscopicity may be useful datasets to evaluate the impact of altering aerosol properties on cloud and precipitation-forming processes under a less polluted environment. While previous studies have examined new particle formation in power plant plumes through ground-based and aircraft measurements[37,63–66], this study presents the first direct observational evidence highlighting the significant impact of SO_2 emissions from coal-fired power plants in greatly enhancing the CCN activity of aerosol particles. We further emphasize the importance of increased aerosol mass burden through new particle formation to be carefully assessed while framing policies to abet the $PM_{2.5}$ reduction plans for polluted coastal clusters across India.

METHODS

The sampling site and measurements are briefly introduced in this section. A detailed description of the measurement site, equations for calculation of condensation and coagulation sinks and, HYSPLIT (Hybrid Single-Particle Lagrangian Integrated Trajectory) model simulated data analysis are described in the supplementary notes.

Sampling site

The measurements of various aerosol properties were carried out with a dedicated inlet protected from insects and other blockages. The instruments were housed in a temperature-controlled laboratory at the Indian Institute of Technology (IIT) Madras (12.990 °N, 80.230 °E; 14 m above sea level), Chennai. The city of Chennai is the fifth most populous city in India, with more than 10 million inhabitants. The measurement site experiences a tropical hot and humid climate, with moderate temperatures during the measurement period (11 April 2020 to 6 May 2020). The average aerosol and meteorological parameters (arithmetic mean ± standard deviation) obtained during the measurements are summarized in the supplementary Table 2.

NR-PM_1 chemical composition measurements

The chemical composition measurements of non-refractory particulate matter with diameters smaller than 1 µm (NR-PM_1)

were carried out using a quadrupole Aerosol Chemical Speciation Monitor (ACSM; Aerodyne Research Inc., USA)[67], which was housed in the laboratory at IIT Madras. The measured chemical composition included organics (Org), sulfate (SO_4), nitrate (NO_3), ammonium (NH_4), and chloride (Cl) at a time resolution of 15 min and unit mass sensitivity. The ACSM uses the same technology as the Aerosol Mass Spectrometer (AMS) without size-resolved data. The sampling system includes a critical orifice of 100 µm diameter, which restricts the air flow rate to 85 cubic centimeters per minute, along with an aerodynamic lens assembly that accelerates the particles into a narrow beam towards the vaporizer, operated at around 600 °C where the non-refractory particles flash-vaporize and then get ionized by 70 eV electron emitting filament. The ions thus formed are detected and analyzed by a quadrupole mass spectrometer.

Even though the ACSM measures PM_1 chemical composition, it is noteworthy to mention that it cannot detect particles below about 40–50 nm[54]. To ensure reliable data quality, all the instrumental calibration and tuning have been conducted carefully with the 300 nm size selected ammonium nitrate and ammonium sulfate particles, following the standard operating procedure recommended by the ACSM manual (Aerodyne Research). The maintenance and calibration method followed during the campaign has been successfully implemented in many of the previous studies[68–70]. The relative ionization efficiency (RIE) for organic aerosol, ammonium, sulfate, and nitrate were 1.4, 5.62, 1.45, and 1.1, respectively, obtained from ammonium nitrate and ammonium sulfate calibration along with a response factor (RF) of 9.06×10^{-11}. A collection efficiency (CE) of 0.5 is applied to all the aerosol species[71]. Maintenance and calibration of the instrument were performed before the campaign's beginning and once during the campaign.

Particle number-size distribution and $PM_{0.5}$ mass derivation

The aerosol number size distribution was measured using a Scanning Mobility Particle Sizer (SMPS, T.S.I. Inc), which comprised a 3082 Electrostatic Classifier with a 3081 Long Differential Mobility Analyzer (L-DMA) and a 3772 butanol-based Condensation Particle Counter (CPC). The measurements were carried out with an aerosol flow rate of 1.0 lpm, and the sheath flow rate through DMA of 6.0 lpm, covering the size range of 9.8–414 nm. The temporal resolution of measurement was 2 min 30 s. A silica gel diffusion dryer was used to maintain the relative humidity of ambient aerosol samples close to ~20% before the sample entered SMPS to avoid any condensation within the instrument. The mass concentration of total $PM_{0.5}$ was derived from the SMPS aerosol number size distribution, assuming a particle density of 1.1 g cm^{-3} [72].

Size resolved CCN measurements

The size-resolved CCN measurements were carried out using a continuous flow stream-wise thermal gradient CCN counter (CCNC, Model 100, Droplet Measurement Technologies, USA) operated in synchronization with an SMPS (T.S.I., 3081 DMA + 3776 CPC), in addition to the one mentioned above. The number concentration of CCN and effective particle hygroscopicity, κ, were retrieved using size resolved CCN measurements as reported by previous studies[73,74]. The investigated particle size ranged from ~20 to 350 nm. The CCNC supersaturation (S) was systematically cycled through 7 different values between 0.06 and 0.8%, which are determined by the temperature gradient (ΔT) in the CCNC column. The critical supersaturation (S_c) and activation diameter (D_{50}) pair, derived from size resolved CCN measurements, was used to calculate the κ. The calibration of the CCN counter was carried out as described in Rose et al.[74].

Only the particles having a critical supersaturation below the S level achieved inside the CCN column activate. Droplets that grow above 1 µm size were considered to be activated and were counted by an optical particle counter. The simultaneous operation of both instruments, CCNC and CPC, yields the activated fraction of each particle size at a given S level ($N_{CCN}(S, D)/N_{CN}$). Plotting this data against particle size for the measured S level gives a scan or activation curve.

The activation curves require correction to measured particle size and corresponding activated fractions. Following Frank et al.[75] and Rose et al.[74], a multiple charge correction was performed on the ratios ($N_{CCN}(S, D)/N_{CN}$) to remove the enhanced activation by multiply charged particles. These corrected ratios were then used to back-calculate the measured diameter of the particles after applying the transfer function correction of the DMA. The supersaturations achieved inside the CCNC column were calculated by periodic calibration experiments using standard ammonium sulfate aerosols (99.99%), following the procedure by Rose et al.[74]. Since the activation of ammonium sulfate aerosol closely follows Köhler theory, the effective supersaturation (S_{eff}) inside the CCNC column can be estimated against the known temperature gradient (ΔT) of the column. S_{eff} showed a consistently good linear relationship with ΔT during calibration experiments. The linear fit of S_{eff} vs ΔT was used for estimating S_{eff} during ambient aerosol measurements.

Black carbon measurements

Atmospheric black carbon (BC) concentrations were measured at 1-min time resolution using the dual-spot model AE-33 Aethalometer (Magee Scientific, Berkeley, USA) at seven different wavelengths (λ) with a flow rate of about 2 lpm[76,77]. The instrument was operated by sampling ambient air with no sample size segregation, and it effectively quantifies BC present in particulate matter of diameters smaller than 1 µm (PM_1). The instrument measures aerosol spectral light absorption, which is converted to BC mass concentrations using the mass absorption cross-section at 880 nm[76]. The multiple scattering enhancement factor "C" (sensitivity) was set to 1.39, and the parameter "Z," which accounts for tangential leakage, was set to 0.01. A default mass absorption cross-section (MAC) value of 7.77 at the wavelength of 880 nm[76] was used for reporting BC concentration. Measurement by the dual-spot Aethalometer (AE-33) is known to minimize the artefacts associated with multiple scattering and filter loadings.

STILT model simulations

We performed simulations using the STILT (Stochastic Time-Inverted Lagrangian Transport) model (version 2.0[78]) to compute the transport of an ensemble of approximately 2000 air particles to the receptor site for 120 h backwards in time, using Global Data Assimilation System (GDAS) data with a spatial resolution of $0.5° \times 0.5°$. For the given meteorological data, one simulation was performed for each ACSM measurement instance. We used the STILT footprints to estimate the average sensitivity of the receptor site to nearby potential sources for high sulfate conditions.

HYSPLIT dispersion model analysis

We used the HYSPLIT (Hybrid Single-Particle Lagrangian Integrated Trajectory) model by NOAA's Air Resources Laboratory for simulating the atmospheric dispersion of the plume arising from the Neyveli thermal power plant on the day of the NPF and growth event. The HYSPLIT model is described in detail elsewhere[79,80]. The NCEP/NCAR Global Reanalysis Data for different pressure levels, having $2.5° \times 2.5°$ resolution, was used as input meteorology for dispersion modeling. The required meteorology files were obtained from the ARL server, which contains 3-d, gridded, ARL/HYSPLIT-format compatible files. The HYSPLIT dispersion model was run using the Neyveli power plant

(11.553 °N, 79.441 °E) as the source, emitting SO_2 continuously at the rate of 822 kg d^{-1} from a stack height of 30–50 m AGL. The emission rate and stack description for the power plant are taken from Fioletov et al.[27]. A simple forward dispersion simulation from the continually emitting source was carried out for 24 h, starting on 30 April 2020 at 12:30 UTC (18:00 IST) and ending on 01 May 2020 at 12:30 UTC (18:00 LT, roughly coinciding with the end of particle growth event). For simplicity, a level terrain was considered, with no wet or dry deposition of the particles emitted from the stack. The vertical top of the model layer was varied between 100–1500 m AGL, and the 24 h average concentrations were obtained within this layer as the model output (Fig. 3f and Supplementary Fig. 8).

TROPOMI satellite data

The TROPOspheric Monitoring Instrument (TROPOMI) onboard the Sentinel-5 Precursor satellite provides high-resolution spectral observations of SO_2 by using the ultraviolet (UV)–visible (Vis) part of the electromagnetic spectrum. The instrument gives daily global coverage data in the UV–Vis region with a horizontal spatial resolution of 3.5 km × 5.5 km. The algorithm for the operational TROPOMI SO_2 retrieval is described in Theys et al.[81]. The level-2 data used in this study can be accessed through the website (http://www.tropomi.eu/data-products/sulphur-dioxide). As per the recommendations mentioned in the product Readme File for SO_2 data, only pixels having qa-value > 0.5 should be used. Therefore, only the pixels for which the data quality is high (qa-value > 0.5) are considered for this study. Instead of mol m^{-2}, the tropospheric SO_2 column number density unit is converted to Dobson Units (DU). The data is then re-gridded into a lat/lon grid to combine the data from multiple orbits from one day into a single daily grid by using the properly weighted area average to calculate the value for each grid cell.

DATA AVAILABILITY

The data used in the manuscript has been deposited in an open research depository as an Igor experiment file, accessible at (https://doi.org/10.6084/m9.figshare.20418960). The aerosol size and chemical composition data, along with the meteorological data used in this manuscript, were obtained from experimental measurements and are summarized in Table S1 in Supporting Information S1. The $PM_{2.5}$ data is obtained from the US Embassy in Chennai and can be accessed at https://www.airnow.gov/international/us-embassies-and-consulates/#India$Chennai. The STILT model (version 2.0[78]) used in the manuscript is openly accessible at https://github.com/uataq/stilt (https://doi.org/10.5281/zenodo.1196561), while the meteorology data obtained from Global Data Assimilation System (GDAS) can be accessed at https://www.ncei.noaa.gov/products/weather-climate-models/global-data-assimilation. The dispersion modeling of SO_2 emission from Neyveli Power Plant was performed using the HYSPLIT dispersion model, accessible at https://www.ready.noaa.gov/hypub-bin/dispasrc.pl. The SO_2 emission rate from the power plant was taken from Fioletov et al. (2020)[27]. The level-2 SO_2 satellite data was retrieved from TROPOMI using the algorithm described in Theys et al. (2017), and the data can be accessed through http://www.tropomi.eu/data-products/sulphur-dioxide. Further, hygroscopicity calculations from size-resolved CCN measurements were performed on MATLAB version R2020b (Mathworks Inc., 2020), licensed under IIT Madras and accessible at https://in.mathworks.com/products/matlab.html. The codes used for calculating and plotting the data are available from the corresponding author upon reasonable request. Figures were prepared using Igor Pro version 8.03 (WaveMetrics Inc.), licensed by SSG and accessible at https://www.wavemetrics.com/downloads/filtered/Igor%20Pro%208.

Received: 12 March 2023; Accepted: 17 July 2023;
Published online: 03 August 2023

REFERENCES

1. Pachauri, R. K. & Reisinger, A. *Climate Change 2007: Synthesis Report. Contribution of Working Groups I, II and III to the Fourth Assessment Report of the Intergovernmental Panel on Climate Change* (IPCC, 2007).
2. Andreae, M. & Rosenfeld, D. Aerosol–cloud–precipitation interactions. Part 1. The nature and sources of cloud-active aerosols. *Earth Sci. Rev.* **89**, 13–41 (2008).
3. Carslaw, K. S. et al. Aerosols in the pre-industrial atmosphere. *Curr. Clim. Change Rep.* **3**, 1–15 (2017).
4. Andreae, M. O. Atmosphere. Aerosols before pollution. *Science* **315**, 50–51 (2007).
5. Hamilton, D. S. et al. Reassessment of pre-industrial fire emissions strongly affects anthropogenic aerosol forcing. *Nat. Commun.* **9**, 3182 (2018).
6. Carslaw, K. S. et al. Large contribution of natural aerosols to uncertainty in indirect forcing. *Nature* **503**, 67–71 (2013).
7. Fan, J., Wang, Y., Rosenfeld, D. & Liu, X. Review of aerosol-cloud interactions: mechanisms, significance, and challenges. *J. Atmos. Sci.* **73**, 4221–4252 (2016).
8. Liu, P. et al. Improved estimates of preindustrial biomass burning reduce the magnitude of aerosol climate forcing in the Southern Hemisphere. *Sci. Adv.* **7**, eabc1379 (2021).
9. Rosenfeld, D. et al. Global observations of aerosol-cloud-precipitation-climate interactions. *Rev. Geophys.* **52**, 750–808 (2014).
10. Wang, Y. et al. Enhancement of secondary aerosol formation by reduced anthropogenic emissions during Spring Festival 2019 and enlightenment for regional $PM_{2.5}$ control in Beijing. *Atmos. Chem. Phys.* **21**, 915–926 (2021).
11. Christensen, M. W. et al. Opportunistic experiments to constrain aerosol effective radiative forcing. *Atmos. Chem. Phys.* **22**, 641–674 (2022).
12. Gunthe, S. S. & Patra, S. S. Impact of international travel dynamics on domestic spread of 2019-nCoV in India: origin-based risk assessment in importation of infected travelers. *Glob. Health* **16**, 1–7 (2020).
13. Gunthe, S. S., Swain, B., Patra, S. S. & Amte, A. On the global trends and spread of the COVID-19 outbreak: preliminary assessment of the potential relation between location-specific temperature and UV index. *J. Public Health* **30**, 219–228 (2020).
14. Krishnamoorthy, S., Swain, B., Verma, R. & Gunthe, S. S. SARS-CoV, MERS-CoV, and 2019-nCoV viruses: an overview of origin, evolution, and genetic variations. *Virus Disease* **31**, 411–423 (2020).
15. Chatterjee, A. et al. High rise in carbonaceous aerosols under very low anthropogenic emissions over eastern Himalaya, India: Impact of lockdown for COVID-19 outbreak. *Atmos. Environ.* **244**, 117947 (2021).
16. Goel, V. et al. Variations in Black Carbon Concentration and Sources During COVID-19 Lockdown in Delhi. *Chemosphere* 129435. https://doi.org/10.1016/j.chemosphere.2020.129435 (2020).
17. Jain, C. D. et al. Phase-wise analysis of the COVID-19 lockdown impact on aerosol, radiation and trace gases and associated chemistry in a tropical rural environment. *Environ. Res.* **194**, 110665 (2021).
18. Jain, S. & Sharma, T. Social and travel lockdown impact considering coronavirus disease (COVID-19) on air quality in megacities of india: present benefits, future challenges and way forward. *Aerosol Air Qual. Res.* **20**, 1222–1236 (2020).
19. Karuppasamy, M. B. et al. Air pollution improvement and mortality rate during COVID-19 pandemic in India: global intersectional study. *Air Qual. Atmos. Health* **13**, 1375–1384 (2020).
20. Kumar, P. et al. Temporary reduction in fine particulate matter due to 'anthropogenic emissions switch-off' during COVID-19 lockdown in Indian cities. *Sustain. Cities Soc.* **62**, https://doi.org/10.1016/j.scs.2020.102382 (2020).
21. Lokhandwala, S. & Gautam, P. Indirect impact of COVID-19 on environment: a brief study in Indian context. *Environ. Res.* **188**, 109807 (2020).
22. Navinya, C., Patidar, G. & Phuleria, H. C. Examining effects of the COVID-19 national lockdown on ambient air quality across urban India. *Aerosol Air Qual. Res.* **20**, 1759–1771 (2020).
23. Singh, R. P. & Chauhan, A. Impact of lockdown on air quality in India during COVID-19 pandemic. *Air Qual. Atmos. Health* **13**, 921–928 (2020).
24. Singh, V. et al. Diurnal and temporal changes in air pollution during COVID-19 strict lockdown over different regions of India. *Environ. Pollut.* **266**, 115368 (2020).
25. Vadrevu, K. P. et al. Spatial and temporal variations of air pollution over 41 cities of India during the COVID-19 lockdown period. *Sci. Rep.* **10**, 1–15 (2020).
26. Kumari, P. & Toshniwal, D. Impact of lockdown measures during COVID-19 on air quality—a case study of India. *Int. J. Environ. Health Res.* **32**, 503–510 (2022).
27. Fioletov, V. et al. Anthropogenic and volcanic point source SO_2 emissions derived from TROPOMI on board Sentinel-5 Precursor: first results. *Atmos. Chem. Phys.* **20**, 5591–5607 (2020).
28. Veeraarasu, P., Satheesh, L. & Dahiya, S. *Emission Watch: Status Assessement of SO_2 Emission and FGD Installation for Coal-based Power Plants In Tamil Nadu* (2021).
29. (CPCB), C. P. C. B. *The Independent Report on "Tamilnadu, Neyveli Boiler Blast" Presented to National Green Tribunal*. (2020).
30. Putaud, J.-P. et al. A European aerosol phenomenology-2: chemical characteristics of particulate matter at kerbside, urban, rural and background sites in Europe. *Atmos. Environ.* **38**, 2579–2595 (2004).
31. Schill, G. et al. Widespread biomass burning smoke throughout the remote troposphere. *Nat. Geosci.* **13**, 422–427 (2020).

32. Yu, H. et al. New particle formation and growth in an isoprene-dominated Ozark forest: from sub-5 nm to CCN-active sizes. *Aerosol Sci. Technol.* **48**, 1285–1298 (2014).
33. Nilsson, E. D. & Kulmala, M. The potential for atmospheric mixing processes to enhance the binary nucleation rate. *J. Geophys. Res. Atmos.* **103**, 1381–1389 (1998).
34. Wehner, B. et al. Horizontal homogeneity and vertical extent of new particle formation events. *Tellus B: Chem. Phys. Meteorol.* **59**, 362–371 (2007).
35. Jähn, M. et al. Investigations of boundary layer structure, cloud characteristics and vertical mixing of aerosols at Barbados with large eddy simulations. *Atmos. Chem. Phys.* **16**, 651–674 (2016).
36. Mahrt, L. Boundary-layer moisture regimes. *Q. J. R. Meteorol. Soc.* **117**, 151–176 (1991).
37. Stevens, R. et al. Nucleation and growth of sulfate aerosol in coal-fired power plant plumes: sensitivity to background aerosol and meteorology. *Atmos. Chem. Phys.* **12**, 189–206 (2012).
38. Mohr, C. et al. Molecular identification of organic vapors driving atmospheric nanoparticle growth. *Nat. Commun.* **10**, 1–7 (2019).
39. Paasonen, P. et al. On the roles of sulphuric acid and low-volatility organic vapours in the initial steps of atmospheric new particle formation. *Atmos. Chem. Phys.* **10**, 11223–11242 (2010).
40. Riipinen, I. et al. The contribution of organics to atmospheric nanoparticle growth. *Nat. Geosci.* **5**, 453–458 (2012).
41. Smith, J. N. et al. Chemical composition of atmospheric nanoparticles formed from nucleation in Tecamac, Mexico: evidence for an important role for organic species in nanoparticle growth. *Geophys. Res. Lett.* **35**, https://doi.org/10.1029/2007GL032523 (2008).
42. Stolzenburg, D. et al. Rapid growth of organic aerosol nanoparticles over a wide tropospheric temperature range. *Proc. Natl Acad. Sci. USA* **115**, 9122–9127 (2018).
43. Yli-Juuti, T., Mohr, C. & Riipinen, I. Open questions on atmospheric nanoparticle growth. *Commun. Chem.* **3**, 1–4 (2020).
44. Jeong, C.-H., Hopke, P. K., Chalupa, D. & Utell, M. Characteristics of nucleation and growth events of ultrafine particles measured in Rochester, NY. *Environ. Sci. Technol.* **38**, 1933–1940 (2004).
45. Erupe, M. E. et al. Correlation of aerosol nucleation rate with sulfuric acid and ammonia in Kent, Ohio: an atmospheric observation. *J. Geophys. Res. Atmos.* **115**, https://doi.org/10.1029/2010JD013942 (2010).
46. Wang, G. et al. Persistent sulfate formation from London Fog to Chinese haze. *Proc. Natl Acad. Sci. USA* **113**, 13630–13635 (2016).
47. Zheng, G. et al. Episode-based evolution pattern analysis of haze pollution: method development and results from Beijing, China. *Environ. Sci. Technol.* **50**, 4632–4641 (2016).
48. Huang, S. et al. Source apportionment of the organic aerosol over the Atlantic Ocean from 53° N to 53° S: significant contributions from marine emissions and long-range transport. *Atmos. Chem. Phys.* **18**, 18043–18062 (2018).
49. Huang, S. et al. Latitudinal and seasonal distribution of particulate MSA over the Atlantic using a validated quantification method with HR-ToF-AMS. *Environ. Sci. Technol.* **51**, 418–426 (2017).
50. Jung, J. et al. Characteristics of methanesulfonic acid, non-sea-salt sulfate and organic carbon aerosols over the Amundsen Sea, Antarctica. *Atmos. Chem. Phys.* **20**, 5405–5424 (2020).
51. Kulmala, M. et al. Formation and growth rates of ultrafine atmospheric particles: a review of observations. *J. Aerosol Sci.* **35**, 143–176 (2004).
52. Pierce, J. R. et al. Nucleation and condensational growth to CCN sizes during a sustained pristine biogenic SOA event in a forested mountain valley. *Atmos. Chem. Phys.* **12**, 3147–3163 (2012).
53. Westervelt, D. M., Pierce, J. R. & Adams, P. J. Analysis of feedbacks between nucleation rate, survival probability and cloud condensation nuclei formation. *Atmos. Chem. Phys.* **14**, 5577–5597 (2014).
54. Liu, P. S. et al. Transmission efficiency of an aerodynamic focusing lens system: comparison of model calculations and laboratory measurements for the Aerodyne Aerosol Mass Spectrometer. *Aerosol Sci. Technol.* **41**, 721–733 (2007).
55. Kanawade, V. P., Sebastian, M., Hooda, R. K. & Hyvärinen, A.-P. Atmospheric new particle formation in India: current understanding and knowledge gaps. *Atmos. Environ.* **270**, 118894 (2022).
56. Yu, H., Ren, L. & Kanawade, V. P. New particle formation and growth mechanisms in highly polluted environments. *Curr. Pollut. Rep.* **3**, 245–253 (2017).
57. Guo, S. et al. Elucidating severe urban haze formation in China. *Proc. Natl Acad. Sci. USA* **111**, 17373–17378 (2014).
58. Rose, D. et al. Cloud condensation nuclei in polluted air and biomass burning smoke near the mega-city Guangzhou, China–Part 2: size-resolved aerosol chemical composition, diurnal cycles, and externally mixed weakly CCN-active soot particles. *Atmos. Chem. Phys.* **11**, 2817–2836 (2011).
59. Rose, D. et al. Cloud condensation nuclei in polluted air and biomass burning smoke near the mega-city Guangzhou, China—Part 1: Size-resolved measurements and implications for the modeling of aerosol particle hygroscopicity and CCN activity. *Atmos. Chem. Phys.* **10**, 3365–3383 (2010).
60. Gunthe, S. et al. Cloud condensation nuclei in pristine tropical rainforest air of Amazonia: size-resolved measurements and modeling of atmospheric aerosol composition and CCN activity. *Atmos. Chem. Phys.* **9**, 7551–7575 (2009).
61. Gunthe, S. et al. Cloud condensation nuclei (CCN) from fresh and aged air pollution in the megacity region of Beijing. *Atmos. Chem. Phys.* **11**, 11023–11039 (2011).
62. Raj, S. S. et al. Planetary boundary layer height modulates aerosol-water vapour interactions during winter in the megacity of Delhi. *J. Geophys. Res. Atmos.* **126**, e2021JD035681 (2021).
63. Brock, C. A. et al. Particle growth in the plumes of coal-fired power plants. *J. Geophys. Res. Atmos.* **107**, 9–14 (2002).
64. Junkermann, W. & Hacker, J. M. Ultrafine particles in the lower troposphere: major sources, invisible plumes, and meteorological transport processes. *Bull. Am. Meteorol. Soc.* **99**, 2587–2602 (2018).
65. Pueschel, R. & Van Valin, C. C. Cloud nucleus formation in a power plant plume. *Atmos. Environ* **12**, 307–312 (1978).
66. Zaveri, R. A. et al. Nighttime chemical evolution of aerosol and trace gases in a power plant plume: Implications for secondary organic nitrate and organosulfate aerosol formation, NO3 radical chemistry, and N2O5 heterogeneous hydrolysis. *J. Geophys. Res. Atmos.* **115**, D12 (2010).
67. Ng, N. L. et al. An Aerosol Chemical Speciation Monitor (ACSM) for routine monitoring of the composition and mass concentrations of ambient aerosol. *Aerosol Sci. Technol.* **45**, 780–794 (2011).
68. Canagaratna, M. et al. Chemical and microphysical characterization of ambient aerosols with the aerodyne aerosol mass spectrometer. *Mass Spectrom. Rev.* **26**, 185–222 (2007).
69. Crenn, V. et al. ACTRIS ACSM intercomparison—Part 1: Reproducibility of concentration and fragment results from 13 individual Quadrupole Aerosol Chemical Speciation Monitors (Q-ACSM) and consistency with co-located instruments. *Atmos. Meas. Tech.* **8**, 5063–5087 (2015).
70. Freney, E. et al. The second ACTRIS inter-comparison (2016) for Aerosol Chemical Speciation Monitors (ACSM): calibration protocols and instrument performance evaluations. *Aerosol Sci. Technol.* **53**, 830–842 (2019).
71. Middlebrook, A. M., Bahreini, R., Jimenez, J. L. & Canagaratna, M. R. Evaluation of composition-dependent collection efficiencies for the aerodyne aerosol mass spectrometer using field data. *Aerosol Sci. Technol.* **46**, 258–271 (2012).
72. DeCarlo, P. F., Slowik, J. G., Worsnop, D. R., Davidovits, P. & Jimenez, J. L. Particle morphology and density characterization by combined mobility and aerodynamic diameter measurements. Part 1: Theory. *Aerosol Sci. Technol.* **38**, 1185–1205 (2004).
73. Petters, M. & Kreidenweis, S. A single parameter representation of hygroscopic growth and cloud condensation nucleus activity. *Atmos. Chem. Phys.* **7**, 1961–1971 (2007).
74. Rose, D. et al. Calibration and measurement uncertainties of a continuous-flow cloud condensation nuclei counter (DMT-CCNC): CCN activation of ammonium sulfate and sodium chloride aerosol particles in theory and experiment. *Atmos. Chem. Phys.* **8**, 1153–1179 (2008).
75. Frank, G., Dusek, U. & Andreae, M. A method for measuring size-resolved CCN in the atmosphere. *Atmos. Chem. Phys. Discuss.* **6**, 4879–4895 (2006).
76. Drinovec, L. et al. The "dual-spot" Aethalometer: an improved measurement of aerosol black carbon with real-time loading compensation. *Atmos. Meas. Tech.* **8**, 1965–1979 (2015).
77. Hansen, A. D., Rosen, H. & Novakov, T. The aethalometer-an instrument for the real-time measurement of optical absorption by aerosol particles. *Sci. Total Environ.* **36**, 191–196 (1984).
78. Fasoli, B., Lin, J. C., Bowling, D. R., Mitchell, L. & Mendoza, D. Simulating atmospheric tracer concentrations for spatially distributed receptors: updates to the Stochastic Time-Inverted Lagrangian Transport model's R interface (STILT-R version 2). *Geosci. Model Dev.* **11**, 2813–2824 (2018).
79. Rolph, G., Stein, A. & Stunder, B. Real-time environmental applications and display system: READY. *Environ. Model. Softw.* **95**, 210–228 (2017).
80. Stein, A. et al. NOAA's HYSPLIT atmospheric transport and dispersion modeling system. *Bull. Am. Meteorol. Soc.* **96**, 2059–2077 (2015).
81. Theys, N. et al. Sulfur dioxide retrievals from TROPOMI onboard Sentinel-5 Precursor: algorithm theoretical basis. *Atmos. Meas. Tech.* **10**, 119–153 (2017).

ACKNOWLEDGEMENTS

S.S.G. gratefully acknowledges funding from the Ministry of Earth Sciences (MoES; sanction number MoES/16/20/12-RDEAS dated 31.Mar.2014), Government of India, for the purchase of the Cloud Condensation Nuclei Counter (CCNC). This work was supported by partial funding from the Ministry of Earth Sciences (MoES; sanction number MoES/16/04/2017-APHH (PROMOTE)), the Government of India,

and the Department of Science and Technology (sanction number DST/CCP/CoE/141/2018C), the Government of India. This work was also partially supported by the U.K. Natural Environment Research Council with grant reference numbers NE/P016480/1 and NE/P016472/1. P.L. acknowledges the start-up funding support from the Georgia Institute of Technology. S.S.G. thankfully acknowledges Alfatech Services, New Delhi, for their generous technical support during the campaign. A. Singh gratefully acknowledges the Prime Minister's Research Fellowship (PMRF) for her doctoral studies. A. Singh was a recipient of IIT Madras's International Immersion Experience (IIE) award to visit the Georgia Institute of Technology, Atlanta, GA, USA for 4 months. U. Panda acknowledges CSIR for fellowship. S.S.G. was a recipient of the Fulbright Fellowship. NO acknowledges valuable support from D. Pallamraju and A. Bhardwaj at P.R.L. V.P.K. acknowledges the University Grants Commission Faculty Recharge Program Fellowship at the University of Hyderabad. The authors are grateful to the three anonymous reviewers for their valuable suggestions and inputs during the review process.

AUTHOR CONTRIBUTIONS

S.S.G. conceived the idea and designed the research. A. Singh conceptualized and planned the field campaign under the supervision of S.S.G., P.L., and R.R.K. A. Singh led the field measurement campaign to collect the extensive field measurement data during the COVID-19 induced lockdown with remote support from S.S.R., S.M.K., U. Panda, S.S., and C.J. V.P.K. carried out the NPF-related data analysis. V.P.K. and S.S.G. conducted NPF data interpretation with critical inputs from F.B. and A.B. U. Panda, S.M.K., S.S.G., and A. Singh conducted the ACSM data analysis. S.H., P.L., S.S.G., J.A., E.R.V., G.M., and L.S. conducted the ACSM data interpretation. A. Singh and SSG led the size-resolved CCN data analysis with help from S.S.R. A. Singh and M.P. conducted the size-resolved CCN data interpretation with help from S.S.G. and P.L. A.V. performed the black carbon data analysis. A.V., S.S.G., V.P.K., and A. Singh conducted the black carbon data interpretation. T.L. performed the STILT simulation and data interpretation with help from P.L. and S.S.G. S.S.G. wrote the first draft and led the manuscript writing by mentoring A. Singh with valuable edits and contributions from V.P.K., N.O., P.L., and R.R. during the manuscript writing. Critical inputs were provided by H.S. and F.B., with inputs and edits to the manuscript further provided by G.M., U. Pöschl, S.T.M., M.O.A., and H.C. All authors read and approved the final manuscript.

COMPETING INTERESTS

The authors declare no competing interests.

ADDITIONAL INFORMATION

Supplementary information The online version contains supplementary material available at https://doi.org/10.1038/s41612-023-00430-2.

Correspondence and requests for materials should be addressed to Pengfei Liu or Sachin S. Gunthe.

Reprints and permission information is available at http://www.nature.com/reprints

Publisher's note Springer Nature remains neutral with regard to jurisdictional claims in published maps and institutional affiliations.